J Mol Model (2006) 12: 468–480
DOI 10.1007/s00894-005-0074-y

ORIGINAL PAPER

Ileana Stoica

Characterization of protein matrix motions in the *Rb. sphaeroides* photosynthetic reaction center

Received: 9 May 2005 / Accepted: 17 October 2005 / Published online: 21 December 2005

Abstract We use Normal Mode Analysis to investigate motions in the photosynthetic reaction center (RC) protein. We identify the regions involved in concerted fluctuations of the protein matrix and analyze the normalized amplitudes and the directionality of the first few dominant modes. We also seek to quantify the coupling of normal modes to long-range electron transfer (ET). We find that a quasi-continuous spectrum of protein motions rather than one individual mode contributes to light-driven electron transfer. This is consistent with existing theoretical models (e.g. the spin-boson/dispersed polaron model) for the coupling of the protein and solvent "bath" to charge separation events.

Keywords Photosynthetic reaction center (RC) · Normal Mode Analysis (NMA) · Electron transfer (ET)

Abbreviations BChl: bacteriochlorophyll · P: primary donor/special pair · B: accessory bacteriochlorophyll · H: bacteriopheophytin · Q: quinone

Introduction

A significant aspect of reactions taking place in protein-cofactor systems was first revealed by the observation of coherent nuclear motions, persisting on the picosecond time scale following impulsive optical excitation, and manifested as oscillations in the transient optical properties of the protein cofactors [1–6]. A complete description of such reactions should therefore consider the possibility of coherent motions of the protein matrix along the reaction coordinate [1]. Conveniently, transient spectroscopy allows the spectrum of low frequency nuclear vibrations that are set in motion by a physiological trigger to be probed experimentally [1–5].

It has also been observed experimentally [1–5, 7, 8] that point mutations in photosynthetic reaction center proteins may alter spectral and redox properties of the main pigments, and thus the photosynthetic process. The most dramatic effects are associated with mutations altering the hydrogen-bonding pattern between the bacteriochlorophylls of the special pair (P) and the surrounding protein [1]. If a change in the protein-cofactor coupling has a strong impact on a vibrational mode, then the protein must take part in the vibration [1]. In fact, even mutations to distant residues not directly bound to P produced changes in the P–P* vibrational spectrum [1], which pointed to the delocalized character of the nuclear motions coupled to the pigment vibrational energies.

Despite its complexity, the purple bacterial RC has become the "hydrogen atom of protein electron transfer" [9], because of the availability of high-resolution crystal structures, and also because of the wealth of spectroscopic data (optical absorption, fluorescence, Raman, EPR, and Stark spectroscopy) collected for its characterization. In addition to amino-acids involved in pigment binding, protonatable residues in the quinone B binding pocket have also been found to be important in photochemistry [9]. Aside from spectroscopical analysis, an essential step in understanding the effect of amino-acid identity on structure and function in the RC protein was the examination of X-ray structures of site-directed mutants or second-site revertants with impaired, restored, or unchanged functionality [9].

Confirmed by experiment, the existence of a coupling between the protein matrix movements and primary charge separation events has been investigated extensively in theoretical studies (see Warshel and Parsons – [10] – for a comprehensive review). The spin boson/dispersed polaron model describes the time evolution of an electron-transfer process in a condensed phase and is due to Warshel and coworkers [11]. Considerable analytical and computa-

The subscripts (e.g. B_M) indicate the subunit L or M (equivalent to A and B, respectively, to designate the active and inactive branch).

I. Stoica (✉)
National Research Council of Canada,
6100 Royalmount Ave.,
Montréal, H4P 2R2, Canada
e-mail: ileana@bri.nrc.ca
Tel.: +1-514-4967831

tional effort has been put into defining the coupling of the pigment Hamiltonian to a continuum of modes within the spin-boson model properly [10]. More recent treatments, also due to Warshel and coworkers, describe the initial electron-transfer steps in the photosynthetic RC by evolving the electron-density matrix via the stochastic Liouville equation [12]. A number of effective vibrational modes are extracted from Molecular Dynamics simulations to express the coupling of protein motions to primary electron transfer [12]. Alternative approaches focus on describing the long-time evolution of the excited state by using a fully quantum mechanical path-integral scheme [13]. The formulation of "dominant pathways" in electron transfer processes [14, 15] brought about the topic of electron tunneling modulation by nuclear dynamics (protein thermal motion).

While a wealth of experimental and theoretical information is available on energy trapping and migration in pigments, not enough is yet known about the protein dynamics. Molecular-dynamics simulations provide an atomically detailed description of the protein motions. However, given the large size of the protein and the necessity for adequate sampling of the protein conformational space, the method is often computationally costly.

In normal-mode analysis, atomic motions are treated as harmonic oscillations, and single point calculations produce modes spanning the full conformational space [16]. Normal-mode analysis provides a description of the dynamics around a local energy minimum. By employing simplified force fields and protein models, which appropriately describe the backbone motion and are sufficient for the characterization of low-frequency motions [17], the coarse-grained normal mode analysis is extendable to systems larger in size than those tractable by all-atom NMA.

The present work consists of a Normal Mode Analysis (NMA) analysis of motional modes in the RC protein of the purple bacterium *Rb. sphaeroides*.

The idea that normal mode/elastic network models can be used to simulate the transition of a protein between two conformations [18] has been explored and applied successfully for proteins as diverse as HIV-1 protease [19], troponin C [16], and SERCA1 Ca-ATP-ase [20]. In extending this analysis to the photosynthetic RC, we seek answers to the following questions:

What are the shapes of low-energy deformations ("soft" directions) in the RC protein of *Rb. sphaeroides*? Are oscillations of the protein matrix coupled to long-range electron transfer (ET)? Does the coupling involve individual modes or a continuous spectrum of protein motions?

We conclude by stating that NMA offers the possibility of selecting a few relevant and easily computable motions from an essentially featureless continuum of modes, expressed in spin-boson models by a spectral density function. We show that these modes are also likely to be involved in the functionality of the protein.

Materials and methods

Normal mode calculations using MMTK

The large size of our model system drastically reduces the computational efficiency of all-atom NMA calculations. We thus limit the current treatment to coarse-grained NM methods such as the approximate normal analysis method developed by Hinsen [17]. The simplified force field used in [17], which does not take into account fundamental properties such as atom type or bond structure, can nevertheless correctly low-frequency modes identify [17]. This is an indication of the fact that the distinction between low- and high-frequency motions is essentially a structural property independent of the details of atomic interactions [17]. While definitely missing out on details of local interactions, coarse-grained NMA can identify protein dynamical domains accurately [17] and capture domain motions that are collective in nature. The large-protein (ATCase) example given in [17] reports the tremendous difference in computation times between the full Cartesian and the coarse-grained mode calculations.

The deformation force field employed in MMTK uses only the C_α atoms of the protein, which, however, are assigned the masses of the whole residues they represent [21]. The functional form of the force field is a sum of pairwise harmonic terms [20]. The NMA tools are implemented in the Molecular Modeling Toolkit (MMTK) [21], which is interfaced with VMD [22] for visualization of the NM trajectories (mode animations). The lowest frequency mode of interest is mode number 7, the first six modes corresponding to the translation and rotation of the protein. Preliminary calculations were done using the MMTK normal mode analysis web server WEBnm@ [23], maintained at the Bioinformatics Platform in Bergen, Norway. Subsequent calculations and more in-depth mode analysis involving higher-frequency modes were carried out on a PC with the freely downloadable packages MMTK and DomainFinder. For atomic displacements and vector field analysis, we used the MMTK input files deformation.py and vector_field.py, with modifications involving customizing some of the parameters (size of the basis set for Fourier Transform, scaling of displacement vector amplitudes, threshold for displacement vector display), to which Python commands were added for calculating normalized atomic displacements. For a ~800 residue protein such as the photosynthetic reaction center, calculating ~200 normal modes takes about 2 min (a little more if visualization and vector field analysis are also needed) on an AMD 950 MHz processor. The procedure is

exquisitely inexpensive computationally if compared to all-atom (AMBER) NM calculations.

Atomic displacements and vector fields

Normalized squared atomic displacements (D_i) for each mode k and each C_α atom were calculated as follows:

$$D^{(k)}i = \|e_{ki}\|^2 \Big/ \sum_j \|e_{kj}\|^2$$

where $\|e_{ki}\|$ is the norm of the eigenvector corresponding to mode k and to the i-th C_α atom, and the sum runs over all residues j in the protein. To facilitate 3D visualization, a vector field representation of the atomic displacements associated with normal modes is available in MMTK as described in [24].

Deformation analysis and definition of the dynamical domains

The DomainFinder program [25] allows for the identification of dynamic domains in proteins. Determination of dynamic domains, based on normal modes, is an effective tool for characterizing the flexibility of a complex protein. The rigid regions are classified according to their global motion and the dynamic domains are composed of residues having the same rigid body motion. The coarseness is the input parameter of the calculation and specifies how similar the rigid-body motions of the different residues should be to consider that these residues form a dynamical domain; thus the smaller the coarseness, the finer the definition of the domains.

Overlap between a displacement vector and the normal modes

The calculation of the dot product (overlap) between a displacement vector and the full set of normal modes identifies which modes contribute most to the given displacement [20]. The displacement vector is in this case the set of coordinate differences:

$$\left\{\mathbf{r}_i^{\mathbf{light}} - \mathbf{r}_i^{\mathbf{dark}}\right\} = \{\Delta \mathbf{r}_i\}$$

where $\boldsymbol{r}_i$ is the C_α -Cartesian positional vector of residue i, and "light" and "dark" represent the structures of the reaction center in its charge-separated (1AIG) and charge-neutral state (1AIJ), respectively (after in vacuo minimization and superposition of protein backbones). In setting up the chain numbering and C_α -trace, only the C_α atoms common to the two structures were considered (chain L: 1–281, chain M: 3–301, chain H: 11–256). The dimensionality of the problem is thus 826.

From the total of 3×826 modes, we calculated 222 for overlap analysis; this was not dictated by computational limitations, but by the choice of keeping consistency with the normal mode analysis done with the WEBnm@ server [23], which calculates 200 modes. If $\boldsymbol{E_k}$:

$$\begin{bmatrix} e_{kl}^{(x)} \\ e_{kl}^{(y)} \\ e_{kl}^{(z)} \\ \cdot \\ \cdot \\ \cdot \\ e_{kN}^{(x)} \\ e_{kN}^{(y)} \\ e_{kN}^{(z)} \end{bmatrix}$$

is the column vector (3N dimensional, N=826) containing the Cartesian components of normal mode $\boldsymbol{k}$ eigenvectors for each C_α atom, and $\boldsymbol{D}$:

$$[\Delta x_1 \quad \Delta y_1 \quad \Delta z_1 \quad . \quad . \quad . \quad \Delta x_N \quad \Delta y_N \quad \Delta z_N]$$

is the difference vector (also 3N-dimensional) between the two conformations, we define the squared overlap between mode $\boldsymbol{E_k}$ and the difference vector $\boldsymbol{D}$ to be the dot product:

$$\mathrm{OV(k)} = (\mathrm{E_k} \cdot \mathrm{D})^2 \Big/ \|\mathrm{E_k}\|^2,$$

where the norm of $\boldsymbol{E_k}$ (sum over all residues) should be 1 if eigenvectors are normalized (they are not in MMTK).

The handling of normal modes for overlap computation was done with an in-house PERL script and Fortran program, which first re-format the data file of Eigenvector Cartesian coordinates printed by MMTK, then compute the mode overlap with the "light"–"dark" difference vectors.

Results and discussion

Characterization of dynamic domains

The analysis of domain flexibility in the RC protein consists of a dynamical domain decomposition, available from the DomainFinder menu. The central parameter which allows a distinction between rigid and more flexible regions is the "domain coarseness" parameter (see the Materials and methods section). In the case of the photosynthetic RC protein, the domain identification was performed with the following values of the coarseness parameter, defined as in [20]: 10, 20, 40 (presented in Fig. 1), 60 and 80. Coarseness values of 40 to 80 produced virtually identical domains (data not shown), which

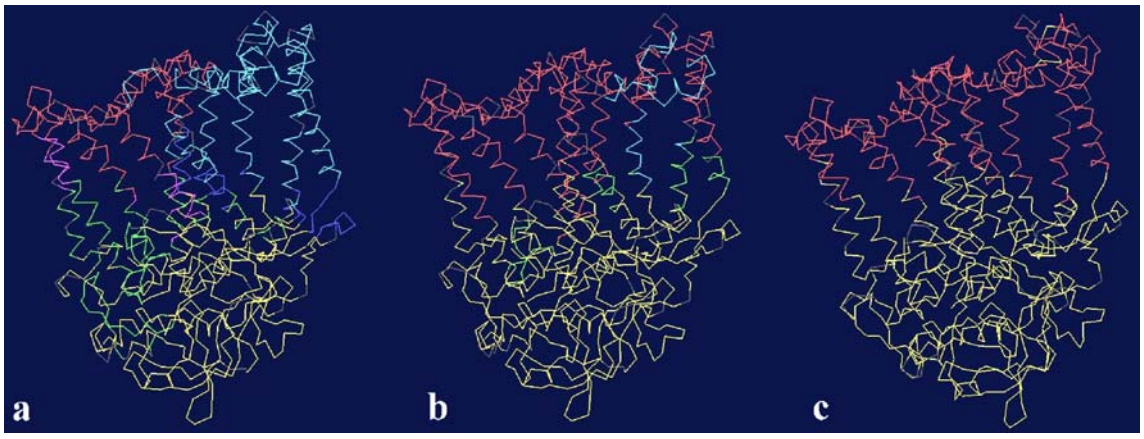

Fig. 1 Dynamical domain decomposition corresponding to normal mode 7 (highest-amplitude mode), for coarseness values of 10 **(a)**, 20 **(b)** and 40 **(c)**. In *yellow* are represented the domains with the highest similarity value (best defined), followed by *red* domains, *green*, *cyan*, *magenta*, etc. *Black* residues do not fall in any of the domains identified. For the sake of clarity, we rotated the left figure 180° about the LM-pseudosymmetry axis, such that the M-subunit is pictured to the right

overlapped with the protein's topological domains: the LM-core and the H subunit.

For deformation energy analysis, 200 normal modes were calculated, out of which modes 7 to 12 were kept for further analysis. Since the deformation energies of modes 7–12 range from 444.7 to 1983.8, the deformation analysis based on these modes was performed with a deformation threshold equal to 1200 [20]. DomainFinder allows for color-coding of the deformation energies and for mapping onto a reference conformation (in this case the PDB structure of 1AIJ).

The results of the deformation analysis presented in Fig. 2 are in good agreement with the domain analysis illustrated in Fig. 1; the best defined domain is the H-subunit, followed by the LM-core, where transmembrane (TM) helices are distinctly more rigid than connecting loops, in particular than lumenal loops. This is also visible from inspection of the crystallographic B-factors (Fig. 2, right). Within the LM-core, the M lumenal loops and helices appear more flexible in the deformation and domain analyses, while the reverse is found from examination of the crystallographic B-factors.

Characterization of global modes in the *Rb. sphaeroides* RC protein

The analysis below focuses on the set of six highest-amplitude collective modes (7 to 12).

Peaks in the atomic square displacements for **mode 7** involve mostly (Fig. 3):

(1) The periplasmic loops and connecting helices “cd” and “ect” in the L-subunit, with a high isolated peak at the

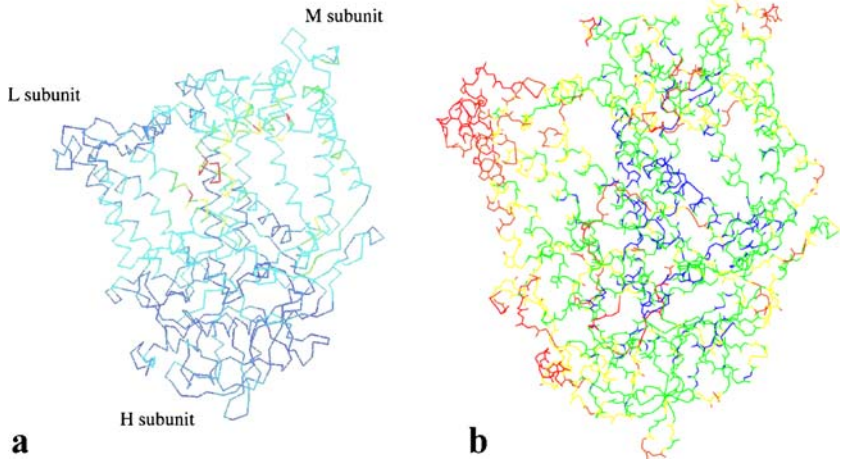

Fig. 2 **a** Deformation analysis in 1AIJ, for the first relevant normal mode (mode 7). For better visualization, the structures are rotated 180° about the membrane axis, such that the M-subunit is pictured to the *right*. *Blue* atoms correspond to small deformation energies, *green* atoms are close to the deformation threshold, and *yellow* and *red* atoms are in particularly flexible regions of the protein. *Blue* and *green* atoms are thus below the deformation threshold and candidates for domains. **b** Color coding of the 1AIJ.pdb B-factor range: *blue*: 10–20, *green*: 20–30, *yellow*: 30–40; *orange*: 40–50; and *red*: B-factor >50

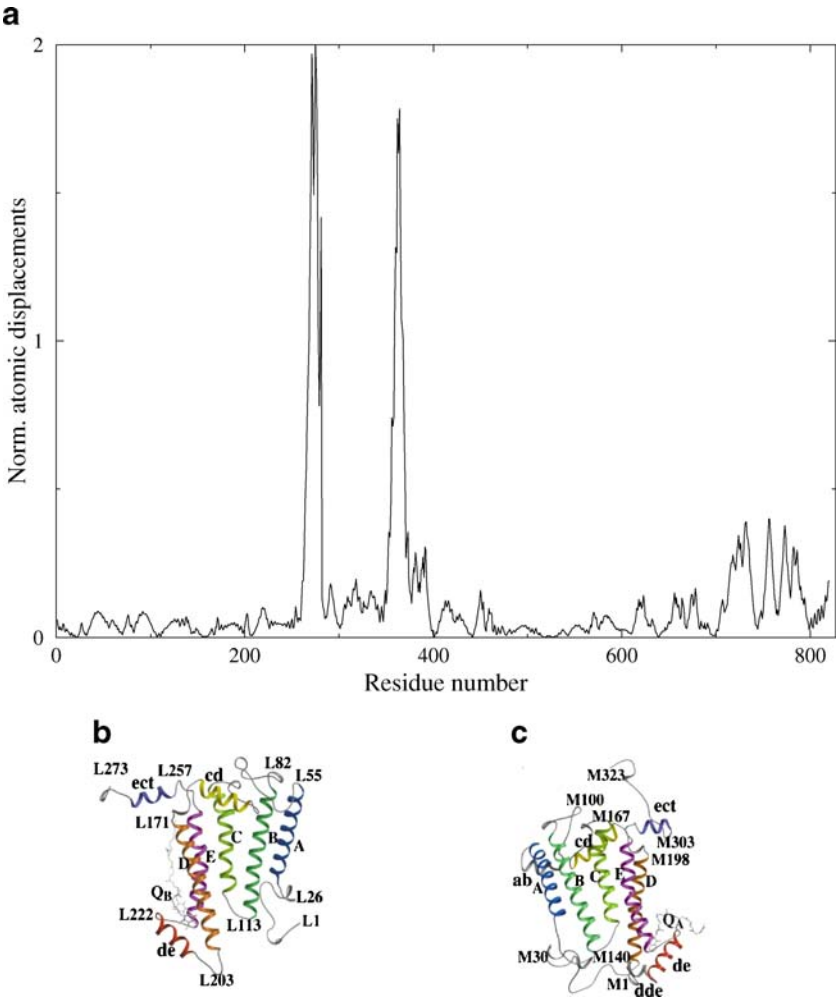

Fig. 3 *Top panel*: normalized atomic squared displacements corresponding to normal mode seven. *Bottom panel*: Topologies of the L-subunit (*left*) and M-subunit (*right*). The dominant features are [9] the five membrane-spanning helices **(A** to **E)**, and the shorter connecting helices on the periplasmic and cytoplasmic sides. Figures reproduced from [9]

C-terminal loop (residues ~270–280). Isolated peaks indicate regions of high local mobility and are not as useful as clusters of smaller amplitude peaks.

(2) The connecting helices "ab", "cd" and "ect" with a strong peak on the N-terminal loop in the M subunit. and

(3) The H-subunit beta-sheets and the cytoplasmic loops connecting the beta-strands in sheet C.

In agreement with the domain analysis and the thermal factors, the backbones of TM helical cores are fairly rigid, while their termini and particularly the connecting interhelical loops exhibit a larger degree of motional freedom.

A vector field representation of mode 7 indicates that the protein undergoes a collective "breathing"-like motion involving mainly the L and M chain periplasmic loops and the H-subunit. Looking down the membrane normal, the

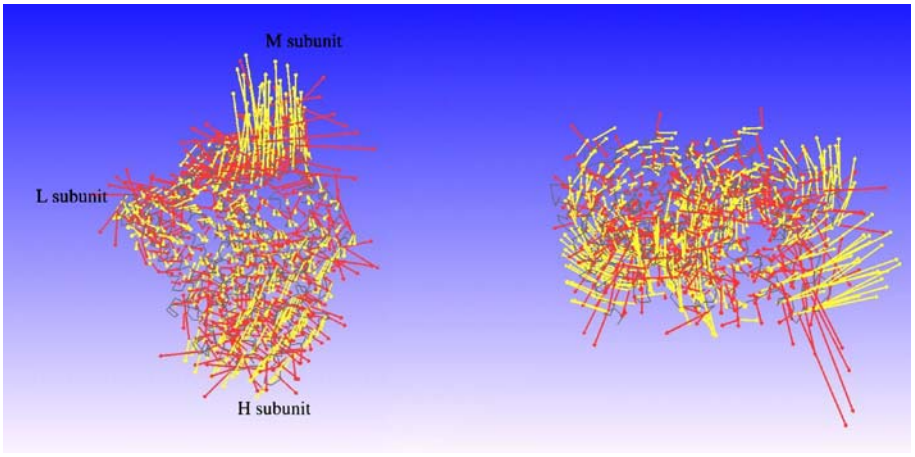

Fig. 4 Vector field representation of mode seven; only vectors with amplitudes greater than a given threshold (chosen as 0.001) are represented (in *red*). Vector curls appear in *yellow*. *Frontal view* (*left*), and *view down* the membrane normal, from the cytoplasmic to the periplasmic side (*right*). For better visualization of motions, we oriented the Figures such that the M-subunit is pictured to the *right*

concerted nature of these motions is even more visible; the motion takes place in a plane perpendicular to the membrane axis (Fig. 4):

Mode 8 describes motions distributed more evenly across the three subunits than mode 8, and involving (Fig. 5):

(1) The L-subunit N-terminal loop
(2) The LM-lumenalloops and connecting helices "ab", "cd" and "ect". and
(3) Most of the H-domain beta sheets and connecting loops, exposed to the cytoplasmic side.

While in mode 7 the lumenal loops in the L and M chains move in opposite directions, in mode 8 they move together, and parallel to the membrane axis. The twisting of the TM helix bundle is best viewed in a lateral representation (Fig. 5).

Mode 9 is similar to mode 7 in that it involves oscillations of the same L- and M-subunit loops, concerted with motions in the cytoplasmic domain of the H-subunit. It also exhibits peaks indicating more localized movements in the L subunit, most likely consisting of torsions around the helical axes.

A vector field representation reveals the similarity between mode 9 and mode 7 (same anti-phase motions of the L and M lumenal loops, in a plane perpendicular to the membrane), but it also emphasizes the more localized character of mode 9 and its smaller amplitudes (Fig. 6):

Mode 10 has similar characteristics to mode 8 in that it involves loops connecting the L-chain TM helices A and B. In a vector field representation looking down the mem-

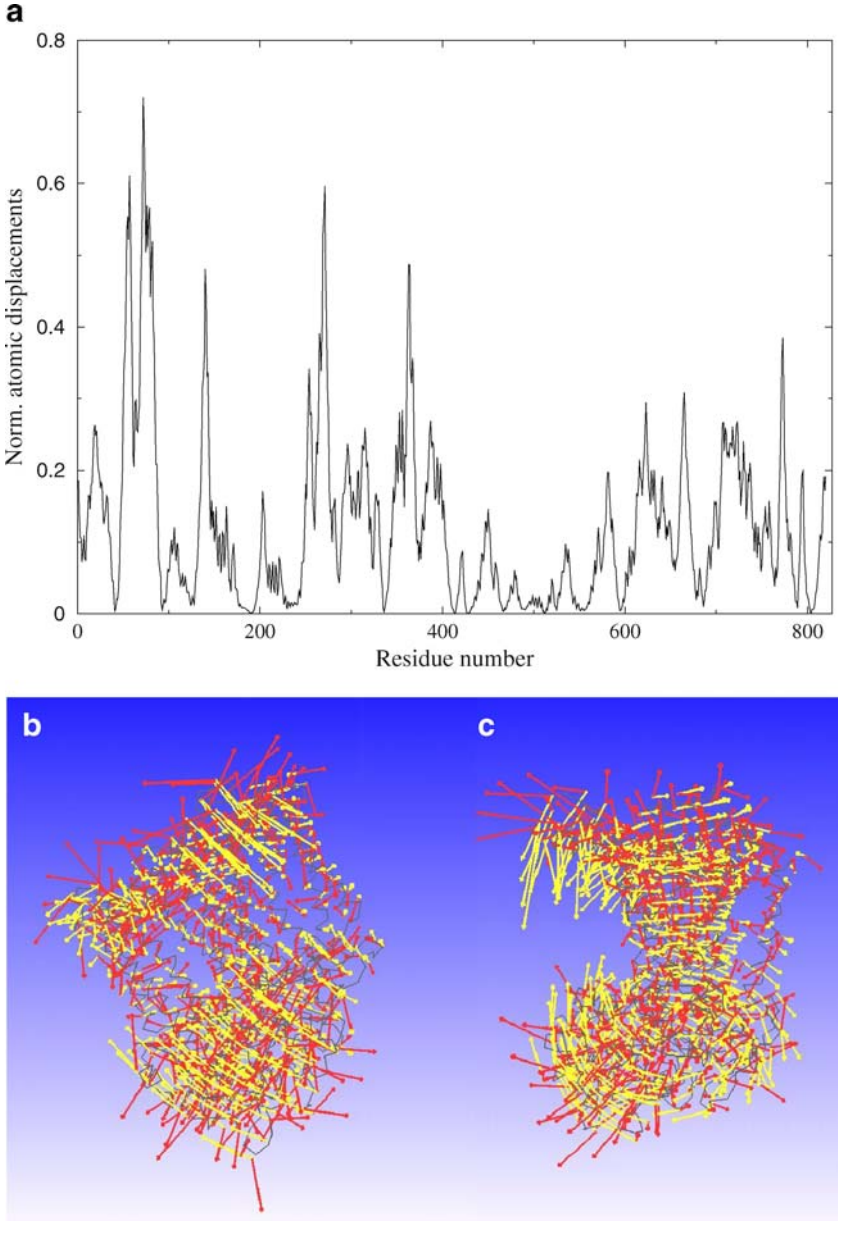

Fig. 5 *Top panel*: normalized atomic square displacements corresponding to normal mode 8. *Bottom panel*: vector field representation of mode 8. *Frontal view* (*left*), and *lateral view* from the M-chain side (*right*). The same observation regarding the orientation of the protein applies as in Fig. 4

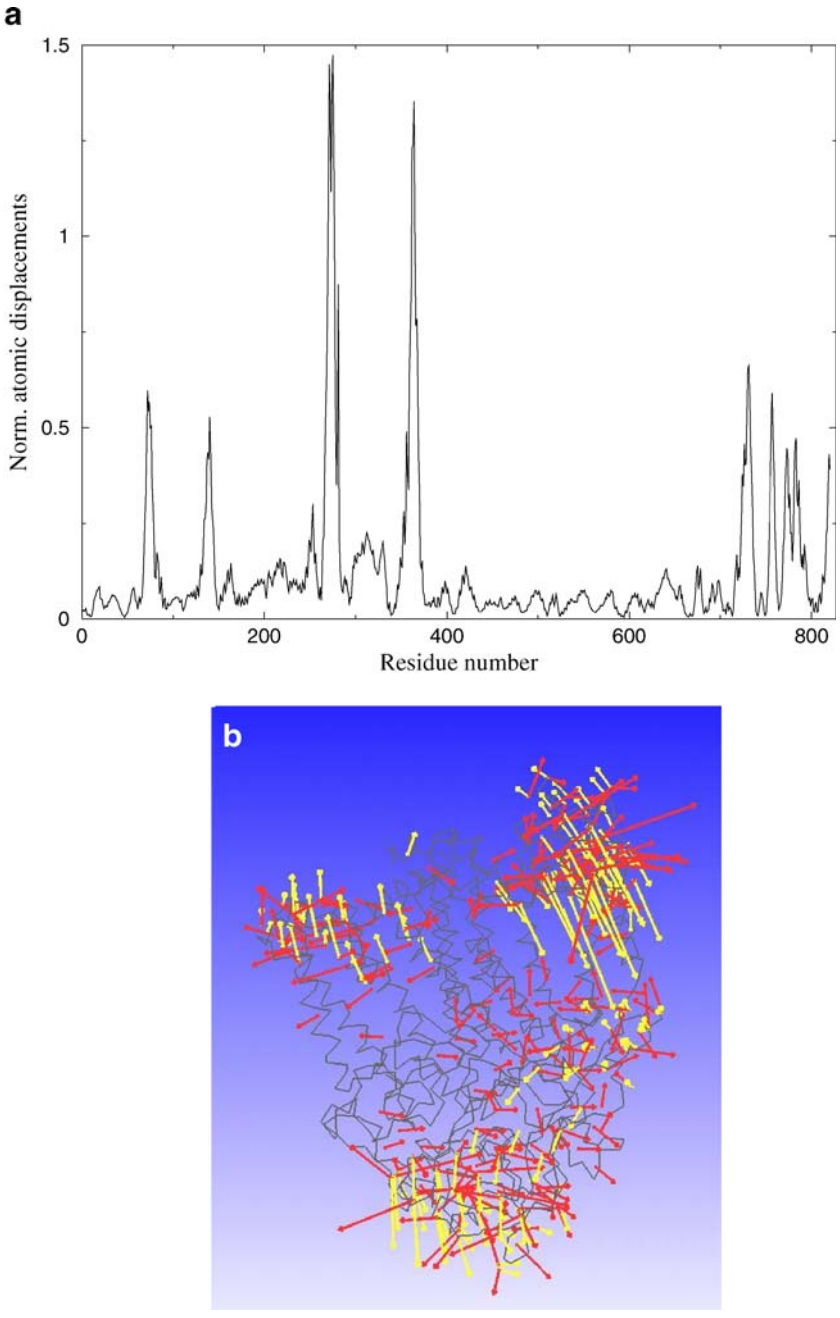

Fig. 6 *Top panel*: normalized square atomic displacements corresponding to normal mode 9. *Bottom panel*: vector field representation of mode 9, *frontal view*

brane axis, it is visible that mode 10 involves both the L- and M- subunits in a concerted fashion, by comparison for instance with **mode 12**, which is more localized (Fig. 7). In mode 12, the oscillations are limited mostly to the L-subunit TM helices A and B.

Mode 11 consists of oscillations of TM helices D of the L and M subunits (Fig. 8), on a direction parallel to the membrane axis.

Investigating the coupling of protein normal modes to long-range electron transfer

Reactive events in proteins may be strongly coupled to a few specific modes of protein motion or they may couple nonspecifically to the dense continuum of protein and solvent modes [26]. Considerable theoretical and experimental work is being devoted to probing the coupling of

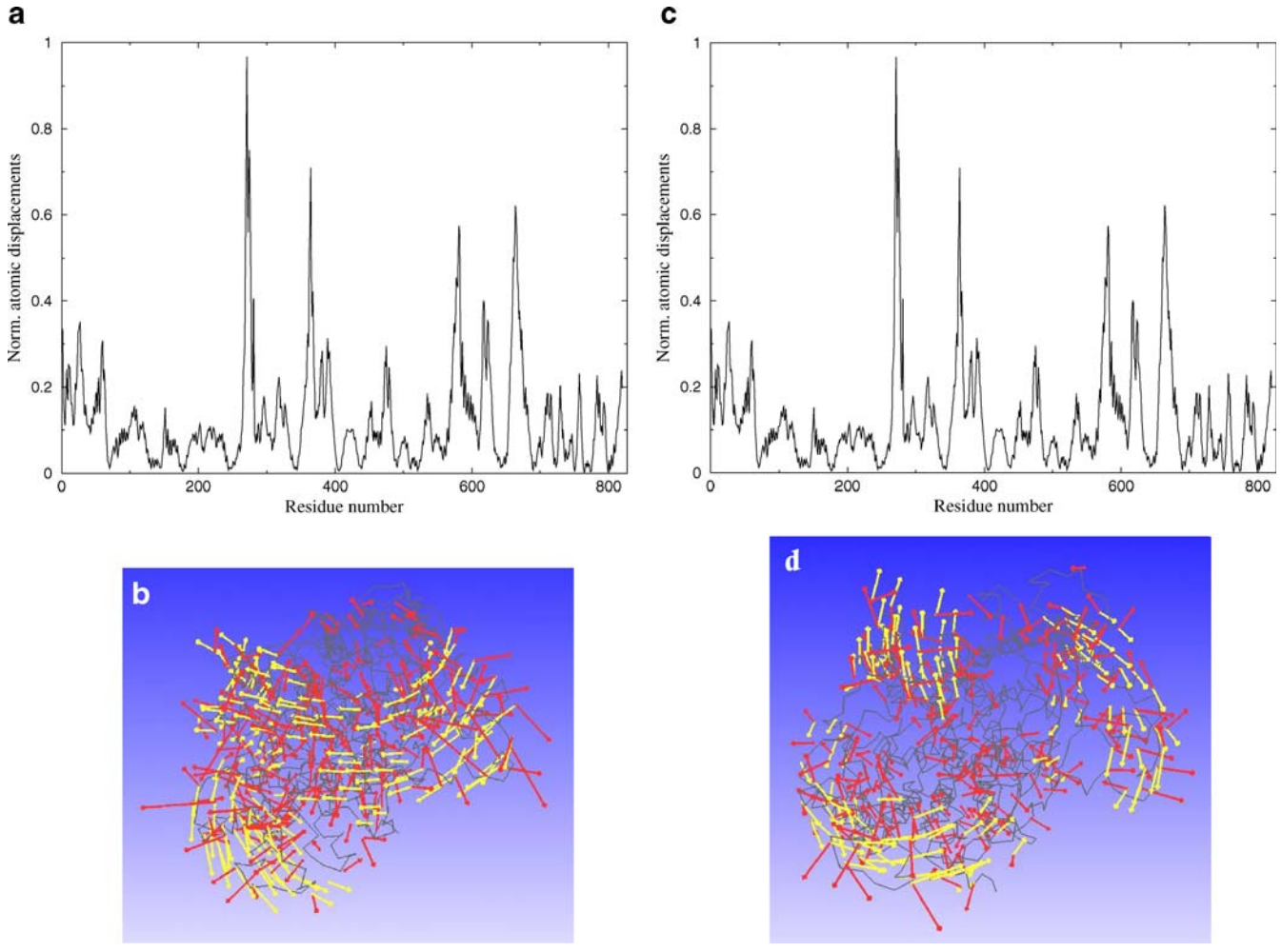

Fig. 7 *Top panel*: normalized square atomic displacements corresponding to normal modes 10 (*left*) and 12 (*right*). *Bottom panel*: vector field representations of modes 10 (*left*) and 12 (*right*); *view down* the membrane normal, from the cytoplasmic to the periplasmic side

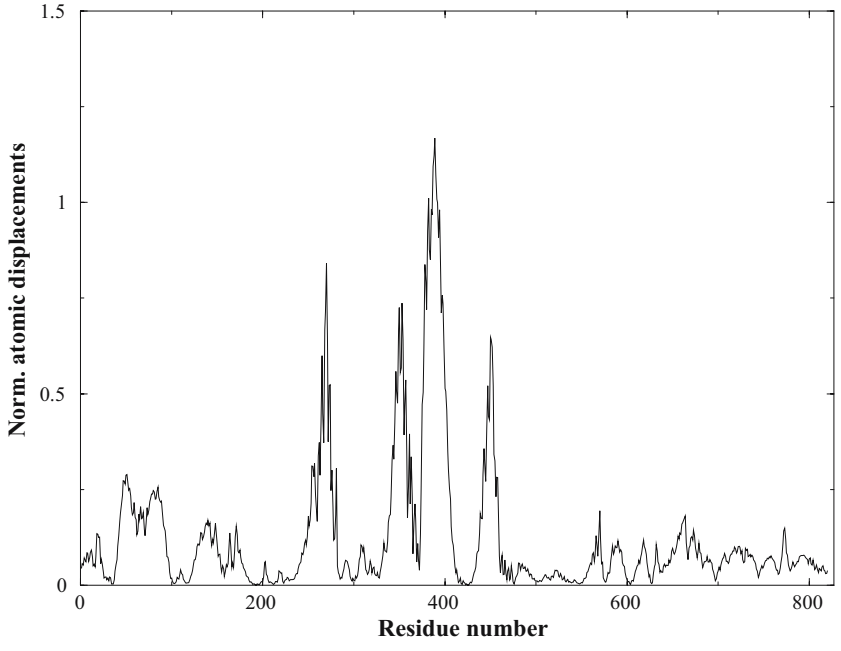

Fig. 8 Normalized square atomic displacements corresponding to normal mode 11

nuclear (protein) motions to the energy transfer and charge separation steps in photosynthetic systems [10].

The vast majority of studies investigating the existence of a coupling between protein motions and electron transfer are focused on the primary electron transfer processes (i.e. from P* to $P^+B_L^-$ to $P^+ H_L^-$, see [10]). These are picosecond-range processes that probably occur before the vibrational levels of the excited state have equilibrated thermally [10]. Evidence for this phenomenon is seen in oscillations in the emission and excited-state absorption following excitation of RCs with subpicosecond flashes [10]. Some of these oscillations have been proposed to involve protein matrix fluctuations [1–6]. Yakovlev et al. [27] also note that the slower motions on the 30 cm^{-1} scale could couple more efficiently to charge separation because they would allow more time for $P^+B_L^-$ to relax.

Kriegl and Nienhaus [28] investigate the role of protein fluctuations in long-range ET during charge recombination $P^+ Q_A^-$–PQ_A, occurring on a ~100 ms time scale, in the WT *Rb. sphaeroides* RC and in four mutant proteins with widely modified free energy gaps. Within the spin-boson model employed, the coupling of the protein vibrational modes to long-range ET was fitted by a smooth function involving exclusively low-frequency vibrations (<30 cm^{-1}), which, authors note, fits nicely with results of MD and path integral simulations [29, 30]. In the study of Parson and Warshel [12], five effective vibrational modes with frequencies in the range 30–235 cm^{-1} were chosen to model the

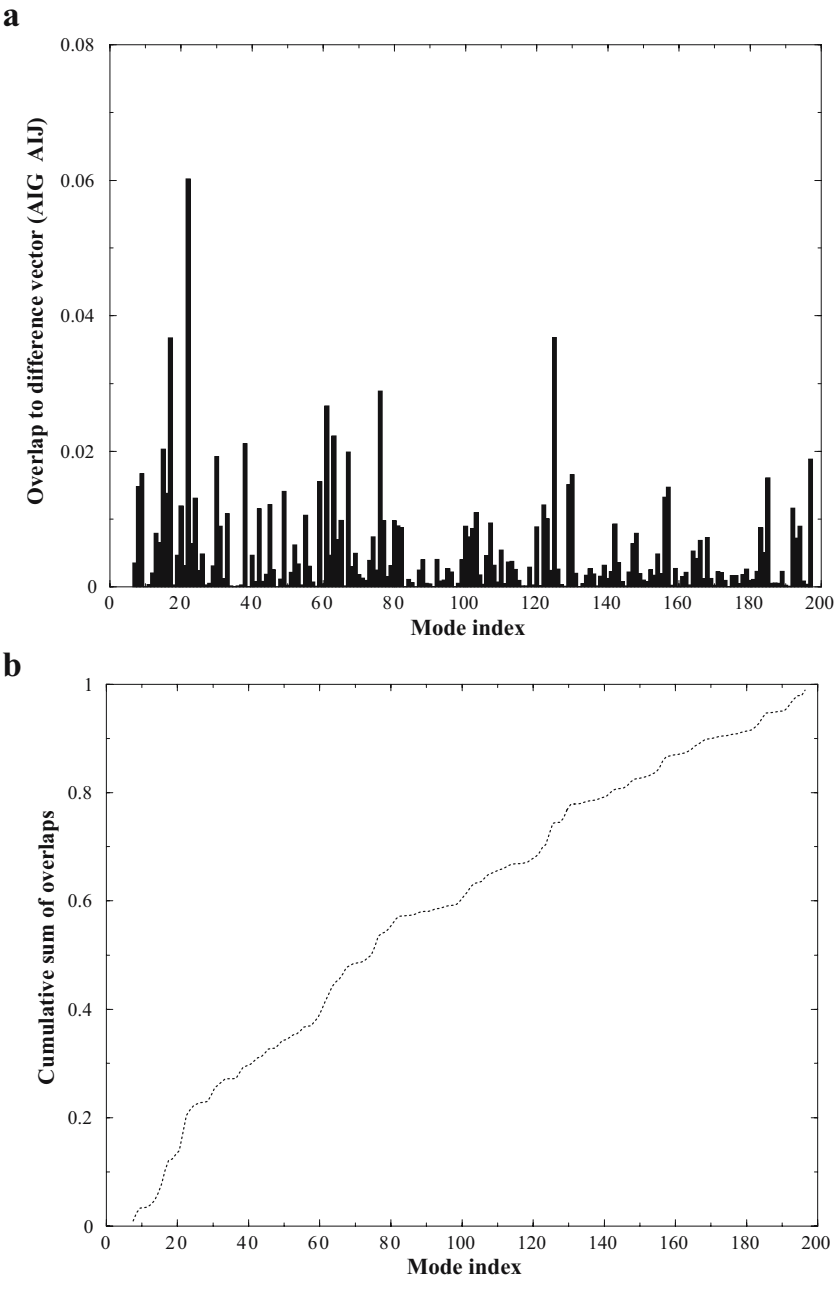

Fig. 9 **a** Contribution of the first 200 normal modes of 1AIJ to the charge neutral—charge separated state transition in the photosynthetic reaction center protein of *Rb. sphaeroides*. The overlap between normal mode eigenvectors and the difference vector {AIG−AIJ} was calculated as described in the Materials and methods section. **b** Cumulative sum over mode overlap values, plotted as a function of the normal mode index

coupling of protein motions to electron transfer. The frequencies and displacements of these vibrations were obtained from the Fourier transform of the autocorrelation function of the energy gap from P* to $P^+B_L^-$, calculated from a 1-ns MD trajectory [12].

We investigate the coupling of individual protein modes to the long-range ET steps, which occur on a time scale several orders of magnitude larger than the primary reactions (~100 μs from Q_A to Q_B).

High-resolution crystal structures of the *Rb. sphaeroides* RC have been reported [31] for both the charge-neutral or "dark" state (DQ_AQ_B, where D is the primary donor), and the charge-separated or "light-adapted" state ($D^+Q_AQ_B^-$). The conformational changes accompanying charge separation in RC have been investigated in detail [31], with a focus on the quinone Q_B binding pocket, as well as on the residues lining the water channels.

Light-driven reactions entail only minor conformational changes in the RC protein, and no intermediates have been identified that would exhibit larger structural changes. However, it is widely accepted that electron transfer is coupled to protein fluctuations [10–12], and that long-range (or "slow") ET in particular couples predominantly to low-frequency protein vibrations [28].

We thus expect that the contribution of protein motions to the dark–light transition will be more evenly distributed over the normal modes than in cases where a large conformational change along a preferential direction accompanies the reaction (as for instance in Ca-binding proteins, see [16, 20]). Such a distribution would also be in agreement with existing theoretical models and representations, most assuming coupling to a continuum of modes. Finally, we note that the existence of large domain fluctuations accompanying a transition, as in the case of Ca-binding proteins, poses in fact a challenge in reproducing actual atomic displacements between the initial and final states from normal mode projections [16]. Normal mode analysis predicts oscillations whose amplitudes correspond to thermal energies kT, while actual (X-ray) atomic displacements can be much larger in some proteins; hence, a scaling problem [16].

In Fig. 9 we present the contribution of the first 200 normal modes computed for the charge-neutral state (1AIJ) to the difference structure {1AIG−1AIJ} (see the Materials and methods section). To find out whether a handful of low-frequency modes, or a wider (quasi-continuous) spectrum of modes participate in the transition, we evaluate per-mode overlap values, as well as a cumulative

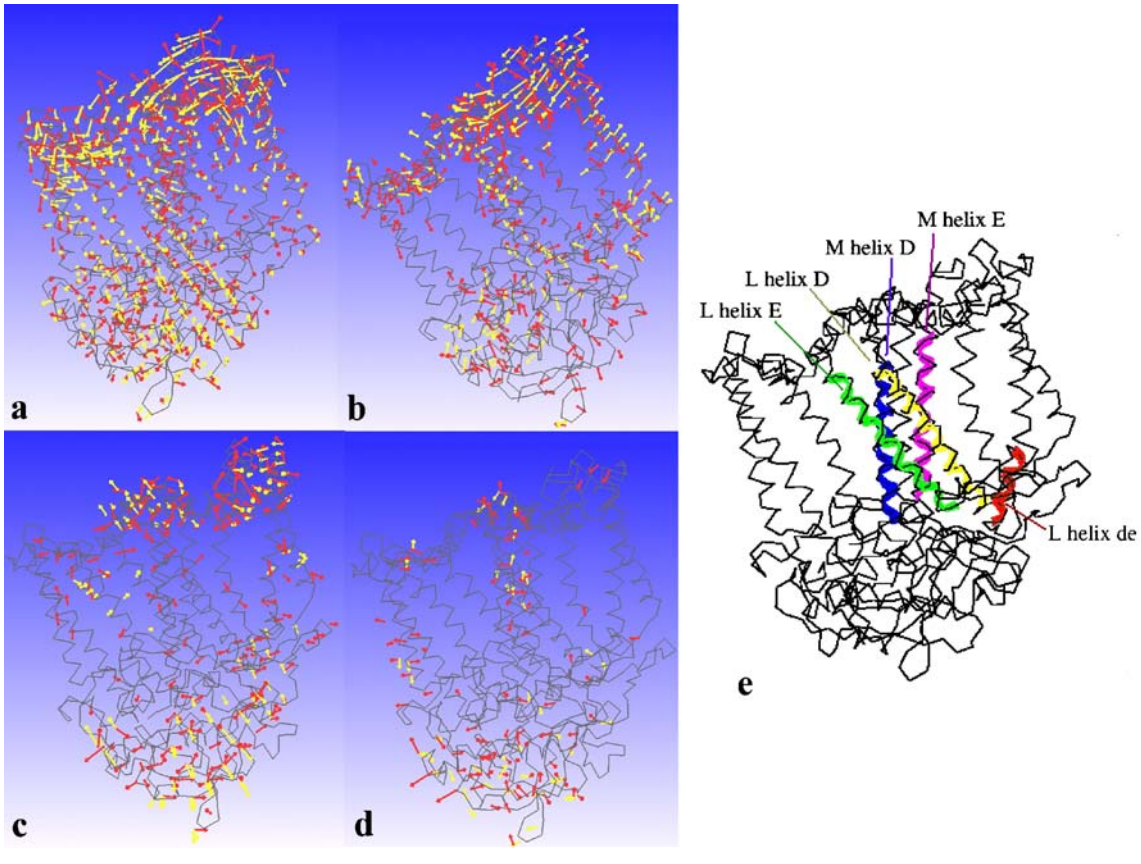

Fig. 10 Vector field representations of modes 17 **(a)**, 22 **(b)**, 38 **(c)** and 63 **(d)**. To facilitate the comparison, only amplitudes above a common threshold of 0.001 are displayed. The structures are rotated 180° about the LM-axis such that the M-subunit is displayed to the *right*. We also include a cartoon of the L helices D, "de", E and of M helices D and E, in *yellow*, *red*, *green*, *blue* and *magenta*, respectively **(e)**. The LM-core appears in the same orientation as in the "vector field" images, to facilitate identification of secondary structure elements

contribution. The absolute values of the NM frequencies have little meaning since no fitting is done to spectroscopically measured frequencies; therefore, the analysis below is based on values relative to the first non-trivial mode (11 cm^{-1} as computed with MMTK).

The protein conformational changes accompanying the light-driven transition have small amplitudes (corresponding to thermal energies). We find, as expected, that these changes are better captured by smaller-amplitude, more localized modes, than by the dominant first modes. As can be seen in Fig. 9, moderate contributions arise from the first six normal modes. Large amplitude motions of the protein, parallel to the membrane axis (mode 8) or perpendicular to it (mode 9) appear to be coupled only to a small degree to changes accompanying the transition. Larger contributions come from modes with higher frequencies: modes 16, 17, 22 (with frequencies 2.5 to 3.2 times higher than that of the first non-trivial mode), modes 38–47 and 59–63 (~4–5 times higher frequencies), as well as mode 125 (10 times faster than the first non-trivial mode).

The cumulative sum of mode overlap values lacks a plateau or "saturation", indicating that a large spectrum of modes couple to the charge separation events, rather than a few high-amplitude modes.

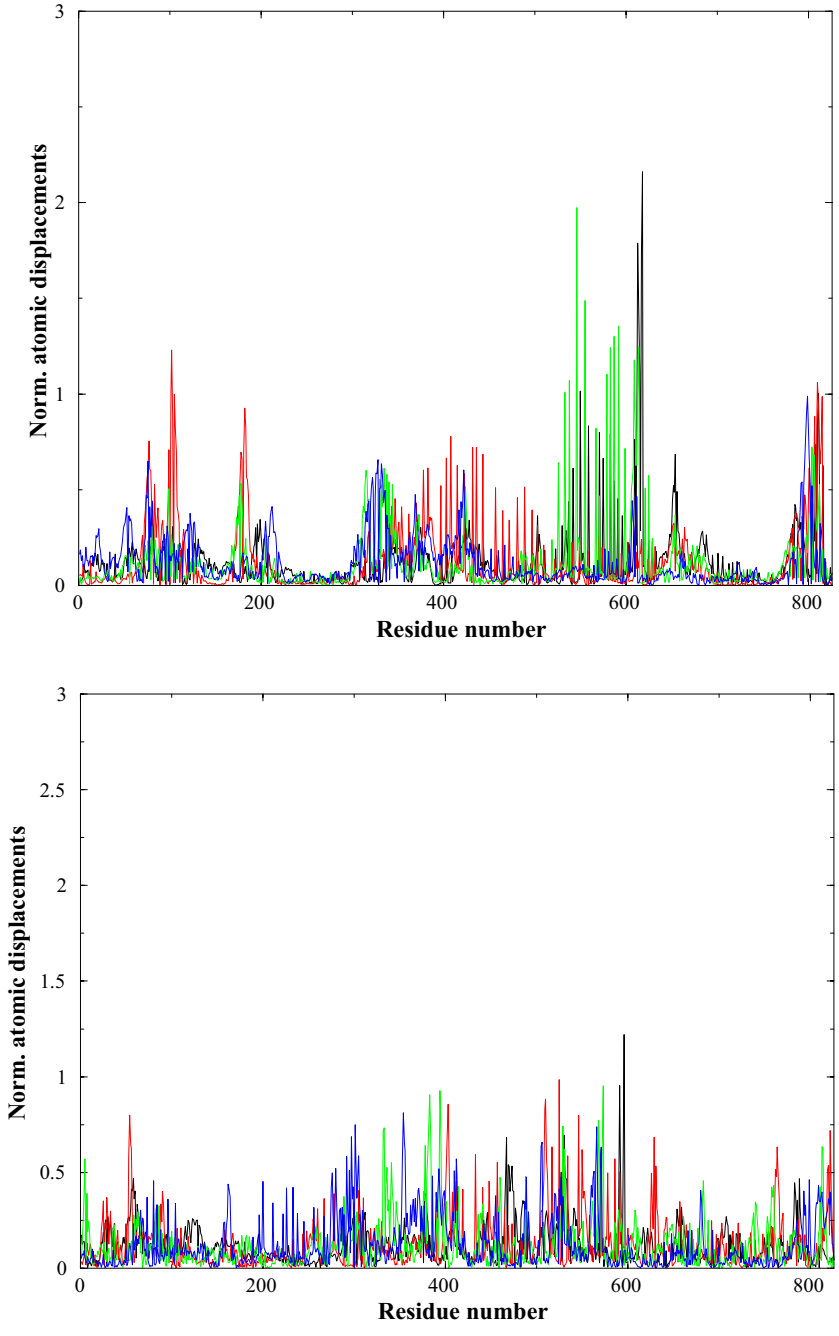

Fig. 11 Normalized atomic square displacements for normal modes coupled to the "dark"–"light" transition in the RC protein of *Rb. sphaeroides*. Unlike for the dominant low-frequency modes which are clearly delineated, a more relevant quantity in the analysis of higher frequency modes would be the envelope over all normal modes within a given frequency range

In Fig. 10 we present a brief description of some of the modes found to be most involved in the "dark"–"light" transition.

As shown in Fig. 10, lower-frequency modes such as 17 and 22 present a collective motion incorporating the L- and M-lumenal loops, as well as parts of the H-subunit. The amplitude of the motion diminishes towards higher-frequency modes (38 and 63), however the motional pattern is remarkably similar throughout the selected modes, which are the subset of modes with the highest "overlap" values (Fig. 9). Interestingly, these modes do exhibit to some extent fluctuations (red arrows in Fig. 11) localized on the L helix "de", proximal to the Q_B binding pocket [31], as well as on L and M helices D, proximal to the special pair towards the periplasm.

The motions on L and M helices are captured as peaks in Fig. 11, which presents normalized square atomic displacements corresponding to some of the modes found relevant to charge separation:

The modes plotted in Fig. 11 show large atomic fluctuations in the M subunit and around L helices D and E, where many mutations responsible for impaired photochemistry have been targeted [9].

Finally, we want to emphasize that the analysis of protein deformations and normal modes in vacuo, with no pigments incorporated in the model, and using an approximate representation of amino acid side-chains in the sense that each C_α caries the weight of the residue it designates is highly schematic as compared to the atomically detailed picture of a protein–pigment complex embedded in a membrane. At the same time, it has been demonstrated that the simplified protein model and force field used in MMTK are able to accurately reproduce the low-frequency modes of large proteins, and that domain motion and deformation analyses have little contributions from degrees of freedom internal to domains [17]. In addition, our focus on high-amplitude global modes is by no means intended to diminish the role of small-amplitude vibrations, localized on side-chains in the immediate vicinity of the special pair, in light-driven reactions.

Conclusion

We find that a wide spectrum of protein normal modes are coupled to the structural changes accompanying the light-driven reactions. The existence of a quasi-continuum of modes rather than of a few dominant modes facilitating the transition is also in agreement with existing theoretical models [10, 11].

Given their manageable number and the accuracy and computational ease of their treatment [21], collective protein motions are amenable to detailed analysis, including visualization of directions and relative amplitudes and mapping onto the 3D structure of the protein. This adds a new, more intuitive dimension to the existing models of electron transfer coupling to protein collective motions.

For microscopic calculations of an electron transfer reaction, classical MD simulations can provide protein vibrational modes that are coupled to the reaction coordinate [10]. Such modes can be incorporated directly in dispersed polaron models [10, 11], or in density matrix treatments as vibrational overlap integrals appearing in the coupling factors [10, 12]. In a similar manner, protein normal modes found to couple to photochemistry can function as suitable candidates for further theoretical manipulation. We conclude by recommending the NM treatment for a "first guess" of protein vibrational modes that can be used to describe the coupling of protein matrix fluctuations to electron transfer in photosynthetic RC-s.

Acknowledgements I wish to acknowledge Dr. Mihaela D Bojin, UC Davis, for a critical reading of the manuscript, for inspiring discussions and in particular for bringing to my attention [28], which I found critical in the interpretation of results.

I am particularly thankful to Dr. Nathalie Reuter, Computational Biology Unit at the Univ. of Bergen, for a critical reading of the manuscript, for helpful suggestions, and for the excellent accessibility and maintenance of the WEBnm@ server [23]. I also wish to thank Prof. Tom Owens, Cornell Univ., for assessing the validity of the questions asked in the present study.

References

1. Rischel C, Spiedel D, Ridge JP, Jones MR, Breton J, Lambry J-C, Martin J-L, Vos MH (1998) Proc Natl Acad Sci USA 95:12306–12311
2. Vos M, Breton J, Martin J-L (1997) J Phys Chem B 101:9286–9820
3. Vos M, Jones MR, Hunter CN, Martin J-L (1994) Proc Natl Acad Sci USA 91:12701–12705
4. Vos M, Jones MR, Hunter CN, Breton J, Lambry J-C, Martin J-L (1994) Biochemistry 33:6750–6757
5. Vos MH, Rappaport F, Lambry J Ch, Breton J, Martin J-L (1993) Nature 363:320–325
6. Fyfe PK, Ridge JP, McAuley KE, Cogdell RJ, Isaacs NW, Jones MR (2000) Biochemistry 39:5953–5960
7. McAuley-Hecht KE, Fyfe PK, Ridge JP, Prince SM, Hunter CN, Isaacs NW, Cogdell RJ, Jones MR (1998) Biochemistry 37:4740–4750
8. Fyfe PK, McAuley-Hecht KE, Ridge JP, Prince SM, Fritzsch G, Isaacs NW, Cogdell RJ, Jones MR (1998) Photosynthesis Research 55:133–140
9. Lancaster CRD, Michel H (2001) Handbook of metalloproteins. In: Messerschmidt A, Huber R, Poulos T, Wieghardt K (eds) Chichester, pp 119–135
10. Warshel A, Parson WW (2001) Quarterly Rev Biophys 34:563–679
11. Warshel A, Hwang JK (1986) J Chem Phys 84:4938–4957
12. Parson WW, Warshel A (2004) J Phys Chem B 108:10474–10483
13. Makri N, Sim E, Makarov DE, Topaler M (1996) Proc Natl Acad Sci USA 93:3926–3931
14. Balabin IA, Onuchic JN (2000) Science 290:114–117
15. Balabin IA, Onuchic JN (1996) J Phys Chem 100:11573–11580
16. Pitici F (2003) Biophys J 84:82–101
17. Hinsen K (1998) Proteins Struct Funct Genet 33:417–429
18. Kim MK, Jernigan RL, Chirikjian GS (2002) Biophys J 83:1620–1630
19. Bahar I, Erman B, Jernigan RL, Atilgan AR, Covell D (1999) J Mol Biol 285:1023–1037
20. Reuter N, Hinsen K, Lacapère JJ (2003) Biophys J 85:2186–2197
21. Hinsen K (2000) J Comput Chem 21:79–85
22. Humphrey W, Dalke A, Schulten K (1996) J Mol Graph 14:33–38

23. Hollup SV, Saelensminde G, Reuter N (2005) BMC Bioinformatics 6:52–70
24. Thomas A, Hinsen K, Field MJ, Perahia D (1999) Proteins Struct Func Genet 34:96–112
25. Hinsen K, Thomas A, Field MJ (1999) Proteins Struct Func Genet 34:369–382
26. Bialek W, Onuchic JN (1998) Proc Natl Acad Sci 85:5908–5912
27. Yakovlev AG, Shkuropatov AC, Shuvalov AV (2000) FEBS Lett 466:209–212
28. Kriegl JM, Nienhaus GU (2004) Proc Natl Acad Sci 101:123–128
29. Warshel A, Chu Z, Parson WW (1989) Science 246:112–116
30. Xu D, Schulten K (1994) Chem Phys 182:91–117
31. Stowell MHB, McPhillips TM, Rees DC, Soltis SM, Abresch E, Feher G (1997) Science 276:812–816